Electrochimica Acta 231 (2017) 247–254

Contents lists available at ScienceDirect

Electrochimica Acta

journal homepage: www.elsevier.com/locate/electacta

Research Paper

High energy lithium ion battery electrode materials; enhanced charge storage via both alloying and insertion processes

Mechthild Lübke[a,b], Dougal Howard[a], Ceilidh F. Armer[b,c], Aleksandra J. Gardecka[a,b], Adrian Lowe[c], M.V. Reddy[d,e], Zhaolin Liu[b], Jawwad A. Darr[a,*,1]

[a] Department of Chemistry, University College London, 20 Gordon Street, London, WC1H 0AJ, UK
[b] Institute of Materials Research and Engineering (IMRE), A*STAR (Agency for Science, Technology and Research), 2 Fusionopolis Way, Innovis #08-03, Singapore 138634, Republic of Singapore
[c] College of Engineering and Computer Science, Australian National University, Canberra, ACT 0200, Australia
[d] Department of Physics, National University of Singapore, Singapore 117542, Republic of Singapore
[e] Department of Materials Science and Engineering, National University of Singapore, Singapore 117576, Republic of Singapore

ARTICLE INFO

Article history:
Received 19 September 2016
Received in revised form 9 February 2017
Accepted 11 February 2017
Available online 16 February 2017

Keywords:
continuous hydrothermal flow synthesis
lithium ion battery
anode
transition metal
alloy

ABSTRACT

A series of nano-sized tin-doped metal oxides of titanium(IV), niobium(V) and vanadium(IV), were directly synthesized using a continuous hydrothermal process and used for further testing without any post-treatments. Each of the as-prepared powders was characterized *via* a range of analytical techniques including powder X-ray diffraction, X-ray photoelectron spectroscopy, transmission electron microscopy and Brunauer-Emmett-Teller surface area measurements, as well as being investigated as an electrode material in a lithium-ion coin cell (*vs* lithium metal). All the tin-doped nanomaterials showed higher specific capacities compared to their undoped metal oxide counterparts. The increased charge storage was discussed to originate from the electrochemical activation of the tin dopant as an alloying material. Overall, this work presents a reliable method of combining stable insertion materials with high capacity tin alloying materials under scaled-up conditions.

1. Introduction

Rechargeable lithium-ion batteries represent the dominant energy storage technology in a range of portable devices from smartphones and laptops to cordless power tools. One desirable attribute for a battery in such devices is a high energy density [1]. For high energy batteries, high capacity and low operating potential (*vs* Li/Li^+) electrode materials, are desirable for the negative electrode of a lithium-ion battery [2]. There are numerous candidate negative electrode materials in lithium-ion batteries that can be classified as storing charge predominately via insertion/intercalation, pseudocapacitive surface reactions, conversion or alloying processes [3]. Insertion of lithium-ions into 1D or 3D structures (intercalation in between the 2D layers) of an electrode material, can involve relatively small volume changes in some host materials, giving generally high cycle stability and moderate to low specific capacities, *e.g.* graphite = 372 mAh g^{-1}, TiO_2 (0.5 M of lithium-ions per 1 M TiO_2) = 168 mAh g^{-1} and lithium titanate LTO = 175 mAh g^{-1} [3]. TiO_2, Nb_2O_5 and VO_2 have attracted attention as lithium-ion battery negative electrodes, due to their relatively low cost and reasonably high theoretical capacities of 175, 200 and 320 mAh g^{-1}, respectively [4–8].

In a previous report by the authors [7], a mixed phase of VO_2 was cycled in the wide potential range of 0.05 to 3.00 V *vs* Li/Li^+ (comparable published literature is usually in the range *ca.* 1.50 to 3.00 V *vs* Li/Li^+); the excellent high power performance (*e.g.* specific capacities of 350 mAh g^{-1} at 0.1 A g^{-1} and 95 mAh g^{-1} at 10.0 A g^{-1}, respectively) was suggested to be due to the material displaying (supercapacitor-like) pseudocapacitive charge storage behaviour under these cycling conditions [9–14]. A similar behaviour was found by the authors in further publication for semicrystalline Nb_2O_5 [6]. Cycling nanosized Nb_2O_5 in a wide potential range of 0.05 to 3.00 V *vs* Li/Li^+ (comparable published literature is usually in the range of *ca.* 1.00 to 3.00 V *vs* Li/Li^+) showed high power performances and additional charge storage at lower potentials, which was largely due to pseudocapacitive charge storage behaviour. In comparison, materials that store charge via conversion and alloying reactions tend to display even

* Corresponding author at: Christopher Ingold Laboratories, Department of Chemistry, University College London 20 Gordon Street, London, WC1H 0AJ. Tel.:+ +44 0 20 7679 4345; Mobile: +44 0 7941 928875.
E-mail address: j.a.darr@ucl.ac.uk (J.A. Darr).
[1] Research webpages http://www.ucl.me.uk.

http://dx.doi.org/10.1016/j.electacta.2017.02.063

higher capacities *e.g.* Fe_2O_3 = 1007 mAh g^{-1}, Si = 3579 mAh g^{-1}, Sn = 993 mAh g^{-1}, and SnO_2 = 782 mAh g^{-1} [15], but tend to display poor cycle life at high active loadings, due to extreme volume/structural changes in the active material during cycling, which damages electrode integrity [16,17].

A number of reports in the literature have sought to develop complex or nanocomposite battery electrode materials, which display a combination of different charge storage mechanisms *e.g.* both insertion and conversion/alloying charge storage mechanisms [18,19]. It is envisaged that such materials can provide a balance between moderate structural changes and reasonably high capacities, which should prolong cycle life stability and possibly high power performance.

In a previous report by the authors [20], Sn^{4+} was successfully doped into anatase TiO_2 and the materials were used as a negative electrode material in a lithium-ion half-cell. In the wide potential window of 0.05 to 3.00 V *vs* Li/Li^+, a significant increase in capacity was observed with increased Sn amount (range of 4 to 15 at% Sn with respect to Ti) because of electrochemical activity resulting from the lithium-ion alloying reactions associated with Sn in the material. The following reactions were proposed for some of the electrochemical lithiation/delithiation processes of such insertion and alloying reactions for Sn doped titanias (Eqs. (1)–(4), apply to titania, whilst Eq. (5) is essentially Eq. (2) expressed for niobium or vanadium oxides as will be discussed later) [3,15,21]:

$$x\mathrm{Li}^+ + \text{electrolyte} + xe^- \rightarrow \text{SEI}\ (x\mathrm{Li}) \quad (1)$$

$$\mathrm{M_yO_z} + x\mathrm{Li}^+ + xe^- \leftrightarrow \mathrm{Li}_x\mathrm{M_yO_z}\ (0 \le x \le 0.5 \text{ for } \mathrm{TiO_2}) \quad (2)$$

$$\mathrm{SnO_2}\ (\text{doped in } \mathrm{M_yO_z} \text{ initially}) + 4\ \mathrm{Li}^+ + 4\,e^- \rightarrow \mathrm{Sn} + 2\ \mathrm{Li_2O} \quad (3)$$

$$\mathrm{Sn} + x\mathrm{Li}^+ + xe^- \leftrightarrow \mathrm{Li}_x\mathrm{Sn}\ (0 \le x \le 4.4) \quad (4)$$

$$\mathrm{M_yO_z} + x\mathrm{Li}^+ + xe^- \leftrightarrow \mathrm{Li}_x\mathrm{M_yO_z}\ (0 \le x \le 2{,}1 \text{ for } \mathrm{Nb_2O_5}, \mathrm{VO_2}) \quad (5)$$

Reaction 1 corresponds to the initial solid electrolyte interphase (SEI) formation during the first and following few cycles. Reaction 2 corresponds to the reversible insertion/deinsertion of lithium-ions into the titania host material. Reaction 4 is the alloying/dealloying reaction of Sn with lithium-ions and this can occur after reaction 3 (formation of metallic Sn and Li_2O). There has been considerable disagreement regarding reaction 3; many researchers support the idea that reaction 3 is irreversible after the first lithiation [22–24]. However, in several electrode materials, higher than expected total reversible lithium-ion charge storage capacities were observed, which suggested partial or fully reversible conversion reactions were likely, *i.e.* the reverse of reaction 3 that would allow SnO_2 to reform during cycling [25–27]. An attempt to confirm this was made by the assistance of ex-situ X-ray photoelectron spectroscopy (XPS) measurements [26,28] and ex-situ high resolution-transmission electron microscopy (HR-TEM) studies [28,29] after the first delithiation step at ca. 3.0 V *vs* Li/Li^+.

Recently, the origin of additional stored capacity for SnO_2 was shown to be a reactive Li_2O layer in the potential range 0.9 to 3.0 V *vs* Li/Li^+ [30]. It was reported that ex-situ TEM measurements were performed at different potentials during cycling, and the highest delithiation activity was observed for Li_2O/LiOH layers with only moderate activity of SnO_x phases. This might be related to the work of Grey et al., who investigated the origin of additional capacity for conversion materials, in this case for RuO_2 [31]. It was shown that the reactivity of lithium hydroxides can provide additional charge storage during the first lithiation, *e.g.* from the reaction for LiOH ($2Li + LiOH \rightarrow Li_2O + LiH$) [31]. The origin of these reactive lithiated layers can be found in the conversion reaction (Eq. (3)) and can also be found in the initial irreversible decomposition of the electrolyte, from which products are adsorbed at the electrode surface (initial formation of LiOH) [32].

In the current study, nanosized $Ti_{0.88}Sn_{0.12}O_2$, $Nb_{1.66}Sn_{0.34}O_5$ and $V_{0.8}Sn_{0.2}O_2$ powders were directly synthesized using a pilot scale continuous hydrothermal flow synthesis (CHFS) reactor and the freeze-dried nano-powder was investigated as potential negative electrode materials for lithium-ion batteries (without any further processing or heat-treatment of the powder whatsoever). The CHFS process is described later, and can be thought of as a rapid and continuous process that mixes supercritical water (in an engineered mixer) with appropriate metal salts in ambient temperature water, to instantly form nanoparticles of the corresponding metal oxides (via a rapid hydrolysis and dehydration reaction) which are collected downstream after in-flow cooling in the process. There are many negative electrode materials for lithium-ion batteries that have been made *via* CHFS type processes, including TiO_2 [8,20], Fe_3O_4 [33], $Li_4Ti_5O_{12}$ [34], semicrystalline Nb_2O_5 [6], VO_2 [7], and layered titanates [35]. The main advantages of using CHFS processes is that materials with small dimensions and narrow size distributions are attainable, which can improve charge transfer/transport processes. The synthesis process also allows very homogenous doping, which can alter the electronic and physical properties of the material under cycling [36]. Different from our previous studies for TiO_2, Nb_2O_5 and VO_2 [6,7,20], where a lab scale reactor was used (production rate <7 g h^{-1}), the materials were synthesized herein using a pilot scale CHFS reactor (used production rate up to 200 g h^{-1} but process capability of 6 Kg per day has been demonstrated for other materials [36]). The nano-sized doped-materials were all investigated electrochemically *via* potentiodynamic and galvanostatic methods in order to assess their performance as stable high energy negative electrode materials. The main aim of the work was to identify if doping high amounts of Sn into different nanosized insertion materials, could increase the specific capacity (due to electrochemical alloying reactions of the dopant at lower potentials vs Li/Li^+).

2. Experimental

2.1. Materials

0.25 M Titanium oxysulphate hydrate ($TiOSO_4$: 29 wt% TiO_2 and 17 wt% H_2SO_4, Sigma Aldrich, Steinheim, Germany) and 0.325 M base potassium hydroxide (KOH, >85%, Fisher Scientific, Loughborough, UK) were used as precursors for titanium oxide synthesis. 0.1 M Ammonium niobate(V) oxalate hydrate (Sigma-Aldrich, >99.99%, Steinheim, Germany) was used for the synthesis of the niobium oxides (no base added). Ammonium metavanadate (0.1 M, >99%, Sigma Aldrich, Steinheim, Germany) was mixed with oxalic acid dehydrate (0.2 M, >99%, Sigma Aldrich, Steinheim, Germany) until the color changed from yellow to dark blue and then used as a V^{4+} precursor solution for the vanadium oxides synthesis [37], (no base added). Tin(IV) sulphate (97%, Acros Organics, Geel, Belgium) was used as a Sn^{4+} precursor in concentrations of 0.055 M, 0.02 M and 0.013 M for the synthesis of $Ti_{0.88}Sn_{0.12}O_2$, $Nb_{1.66}Sn_{0.34}O_5$ and $V_{0.8}Sn_{0.2}O_2$, respectively.

2.2. General synthesis process

Nanosized transition metal oxides were synthesized using a pilot-scale continuous hydrothermal flow synthesis (CHFS) reactor utilizing a confined jet mixer (CJM), the design of which is fully

described elsewhere [38]. In the CHFS process herein, a stream of cold water was pumped (via pump 1 at 400 mL min^{-1}) and heated in flow to well above its critical temperature (heated to 450 °C at 24.1 MPa). This supercritical water stream was then mixed in a CJM with an ambient temperature metal salt/base aqueous precursor feed mixture (T = 20 °C, P = 24.1 MPa), resulting in the instantaneous formation of the corresponding nanocrystallite metal oxide in the water (see reactor scheme in supplementary Fig. S1). In this case, the ambient temperature metal salt precursor and DI water or base were first premixed in flow in a low volume T-piece (0.25" internal diameter) at ambient temperature using pumps 2 and 3, respectively (both at 200 mL min^{-1}). This combined metal salt/base aqueous precursor feed mixture (at 400 mL min^{-1}) entered into the side arms of the CJM, where it rapidly mixed with the inner supercritical water feed, forming a turbulent jet. A nucleation dominated reaction occurred (temperature of *ca.* 335 °C after rapid mixing) as a result of the metal salts being supersaturated upon mixing with supercritical water, while being simultaneously and instantly hydrolysed and dehydrated [39]. The reaction slurry had a residence time of *ca.* 6.5 s after which time it was then cooled in flow (via a pipe-in-pipe heat exchanger). The slurry then passed through a back-pressure regulator (BPR, Tescom series) where it was collected; the slurry was then concentrated with a centrifuge (4500 rpm, 10 minutes) with several washings of DI water and further re-centrifuged to a thick wet sludge that was freeze-dried (Virtis Genesis 35XL) by slowly heating up from -60 °C to 25 °C, over 24 h under vacuum of < 100 mTorr.

2.3. Characterization

Powder X-ray diffraction (XRD) patterns of all the niobium and titanium oxides were obtained on a STOE diffractometer using Mo-Kα radiation (λ = 0.71 Å) over the 2θ range 4 to 40°, with a step size of 0.5° and step time of 20 s. Powder X-ray diffraction (XRD) patterns of the vanadium oxides were obtained on a Bruker D4 diffractometer using Cu-Kα radiation (λ = 1.54 Å) over the 2θ range of 20–80° with a step size of 0.05° and a step time of 2 s. X-ray photoelectron spectroscopy (XPS) measurements were collected using a Thermo Scientific K-alpha spectrometer using Al-Kα radiation and a 128-channel position sensitive detector. The XPS spectra were processed using CasaXPS™ software (version 2.3.16) and the binding energy scales calibrated using the adventitious C 1 s peak at 285 eV.

The size and morphology of the crystallites were determined by transmission electron microscopy (TEM) using a Jeol JEM 2100–LaB_6 filament. The system was equipped with Agatan Orius digital camera for digital image capturing. Samples were prepared by briefly ultrasonically dispersing the powder in methanol and pipetting drops of the dispersed sample on a 300 mesh copper film grid (Agar Scientific, Stansted, UK). Energy dispersive X-ray (EDX) analysis was carried out using an Oxford Instruments X-Ma N80-T Silicon Drift Detector (SDD) fitted to the transmission electron microscope and processed using AZtec™ software. Brunauer-Emmett-Teller (BET) surface area measurements were carried out using N_2 in a micrometrics ASAP 2020 Automatic High Resolution Micropore Physisorption Analyzer. The sample was degassed at 150 °C (12 h) before measurements.

2.4. Electrochemical testing

The nano-sized sample was used as the electrode active material without any heat-treatment. The slurry for the electrode was prepared with a content of 70 wt% active materials, 20 wt% conductive agent (carbon black, Super P™, Alfa Aesar, Heysham, UK) and 10 wt% polyvinylidene fluoride, (PVDF, PI-KEM, Staffordshire, UK). 5 wt% PVDF was dissolved in N-methyl-2-pyrrolidone (NMP, Sigma Aldrich, St. Louis, USA) for at least 1 h at room temperature before adding the active material and conductive agent. More NMP was added accordingly to reach optimum viscosity. The mixtures were milled and the slurry was cast on a copper foil (PI-KEM, Staffordshire, UK) and dried in an oven at 70 °C for 1 hour and then left overnight at room temperature. Electrodes with a diameter of 16.0 mm were punched out, pressed and dried overnight at 70 °C. The electrodes had an active material mass loading of 2.1 ±0.2 mg cm^{-2}, 1.7 ±0.2 mg cm^{-2} and 1.0 ±0.2 mg cm^{-2} for $Ti_{0.88}Sn_{0.12}O_2$, $Nb_{1.63}Sn_{0.34}O_5$ and $V_{0.8}Sn_{0.2}O_2$, respectively.

Electrochemical experiments were performed using two-electrode CR2032-type coin cells, which were assembled in an argon-filled glovebox (MB150B-G, MBraun, Garching, Germany) with O_2 and H_2O limited to below 3 ppm. The counter electrode was lithium metal foil. The separator (glass microfiber filters, Whatman, Buckinghamshire, UK) was saturated with an organic electrolyte of 1 M $LiPF_6$ in ethylene carbonate/dimethyl carbonate (1:1 v/v, Merck Selectipur LP40, Darmstadt, Germany).

C-rate tests and long-term cycling were performed using a Maccor battery tester (Model 4200, Maccor Inc., Oklahoma, USA) at room temperature. The specific current rates were set between an applied current of 100 to 2,000 mA g^{-1} in the potential range 0.05 to 3.00 V *vs* Li/Li^+. The electrochemical performance was investigated by cyclic voltammetry (CV) in the same potential range with a scan rate of 0.1 mV s^{-1} using a galvanostat/potentiostat (PGSTAT302, AUTOLAB, Metrohm, Utrecht, Netherlands). The specific current and specific capacities were calculated based on the mass of active material for each electrode.

3. Results and discussion

$Ti_{0.88}Sn_{0.12}O_2$ (yield >90 %, production rate on flow reactor of *ca.* 200 g h^{-1}), $Nb_{1.66}Sn_{0.34}O_5$ (yield >90 %, production rate *ca.* 130 g h^{-1}) and $V_{0.8}Sn_{0.2}O_2$ (non-optimised yield >56 %, production rate

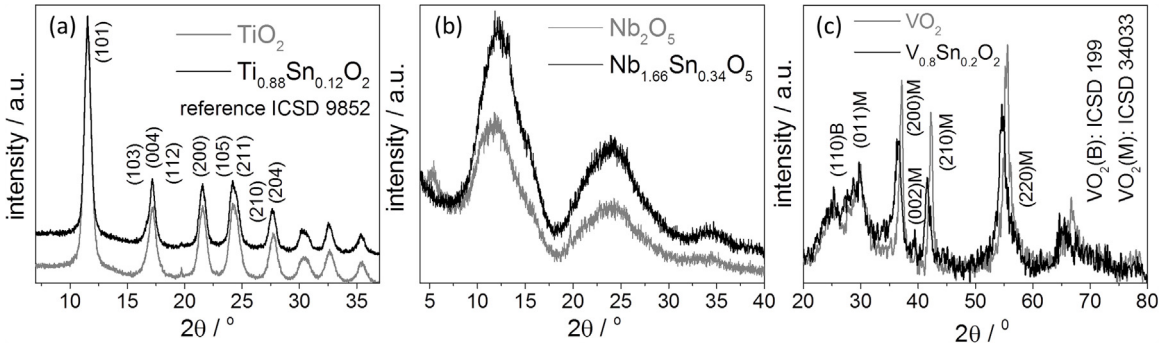

Fig. 1. XRD data plots (Mo-source) of a) $Ti_{0.88}Sn_{0.12}O_2$ and b) $Nb_{1.66}Sn_{0.34}O_5$. c) XRD data plot (Cu-source) of $V_{0.8}Sn_{0.2}O_2$.

ca. 65 g h^{-1}) were collected as free flowing powders after freeze drying and directly used for further investigation. The doped titania and niobia powders were slightly yellow and the doped vanadia powder was dark blue in colour. The yield was low for the vanadium dioxide synthesis as it was not optimized in this first attempt and can be increased in the future by the use of an appropriate base or indeed an alternative precursor that is less soluble [38].

All materials were investigated *via* PXRD, as detailed in Fig. 1. No evidence of a separate phase such as SnO_2 phase was detected in any of the patterns for the as-prepared nanopowders. The titania-based materials were identified as phase pure anatase, which was similar to that reported previously [20]. For the niobium based oxides, the PXRD data reflections were very broad, which indicated a small sized, semi-crystalline material [6]. For the vanadium oxides, there was no clear indication of any V_2O_5 phase, however, the patterns were very broad and suggested a mixture of monoclinic VO_2(M) and metastable VO_2(B) phase. In the current study, as a higher mixing temperature was used compared to the author's previous report on the synthesis of thermochromic VO_2 (335 vs 305 °C), the sample appeared to contain relatively less of the metastable low temperature VO_2(B) phase [7].

The particle morphology of $Ti_{0.88}Sn_{0.12}O_2$, predominantly consisted of *ca.* 8 nm rounded particles (Fig. 2a and b). EDX analysis of the same sample, suggested a homogenous distribution of the Sn in the sample and a Sn:Ti atomic ratio of 11.9:88.1, which was consistent with the results obtained by XPS (supplementary Fig. S2). XPS measurements suggested that the metals were exclusively found in the 4+ oxidation state (Ti^{4+} and Sn^{4+}). The BET surface area was found to be 230 m^2 g^{-1} for undoped TiO_2 nanoparticles and 186 m^2 g^{-1} for $Ti_{0.88}Sn_{0.12}O_2$, which was close to the expected value of 198 m^2 g^{-1} for the latter (based on the hard sphere model value of 8 nm).

The particle morphology for $Nb_{1.66}Sn_{0.34}O_5$ predominantly consisted of nanoparticles with a defective "spherical" morphology of *ca.* 15 nm in size. According to TEM images, there were no detectable interlayer d-spacings, which were attributed to the highly defective structure (Fig. 2c and 2d). EDX measurement analysis of the sample showed a homogenous distribution of the Sn in the sample and suggested a Sn:Nb atomic ratio of 17:83, which was slightly higher compared to the results on the surface of the material obtained by XPS (15.7:84.3, supplementary Fig. S3). XPS measurements showed only Nb^{5+} and Sn^{4+} as oxidation states. The BET surface area was 183 m^2 g^{-1} for undoped Nb_2O_5 and 167 m^2 g^{-1} for $Nb_{1.66}Sn_{0.34}O_5$.

For $V_{0.8}Sn_{0.2}O_2$, the particle morphology predominantly consisted of a mixture of defective spherical particles as well as thin sheets with lengths less than 1 μm, as observed in Fig. 2e and f (and in supplementary Fig. S4). EDX measurements over the surfaces of either the sheets or the defective spheres, suggested a Sn:V atomic ratio of 20.5:79.5, which was consistent with the results obtained by XPS investigations (supplementary Fig. S5). The XPS data suggested the surface of the sample was composed of Sn^{4+}, V^{4+} and some V^{5+} in an atomic ratio of 20:61:18. As there was no detectable impurity phase in the PXRD data, it was concluded that there was surface oxidation occurring [40]. The BET surface area was 22 m^2g^{-1} for undoped VO_2 and 24 m^2g^{-1} for $V_{0.8}Sn_{0.2}O_2$.

Fig. 3 shows the cyclic voltammetry (CV) data; where an irreversible minor peak was observed at *ca.* 0.6 V *vs* Li/Li^+ for all materials, which was assumed to be due to the reaction of the electrolyte with the carbon additive in the electrode (solid electrolyte interphase formation) [41,42]. For the $Ti_{0.88}Sn_{0.12}O_2$ sample in a half-cell configuration, there were reversible redox peaks at 2.1 and 1.6 V *vs* Li/Li^+, as expected for lithium-ion insertion/extraction into anatase TiO_2 [8,20,43,44]. For the $Nb_{1.66}Sn_{0.34}O_5$ half-cell, the electrochemical activity of the active material was extended beyond the typical range for the redox couple of $Nb^{5+} \leftrightarrow Nb^{3+}$ (1.1 ± 0.1 to 1.8 V vs Li/Li^+ [45–50]) and the CV profile did not show clear insertion peaks at well-defined potentials *vs* Li/Li^+, which was consistent with the author's previous results for negative electrode nanomaterials with high surface area [6]. The CV inset in Fig. 3a and b, clearly showed additional lithium-ion storage at lower potentials and higher lithium-ion release at *ca.* 0.5 V *vs* Li/Li^+ for $Ti_{0.88}Sn_{0.12}O_2$ and $Nb_{1.66}Sn_{0.34}O_5$ in comparison with their undoped counterparts, which showed the electrochemical activity of the Sn^{4+} dopant.

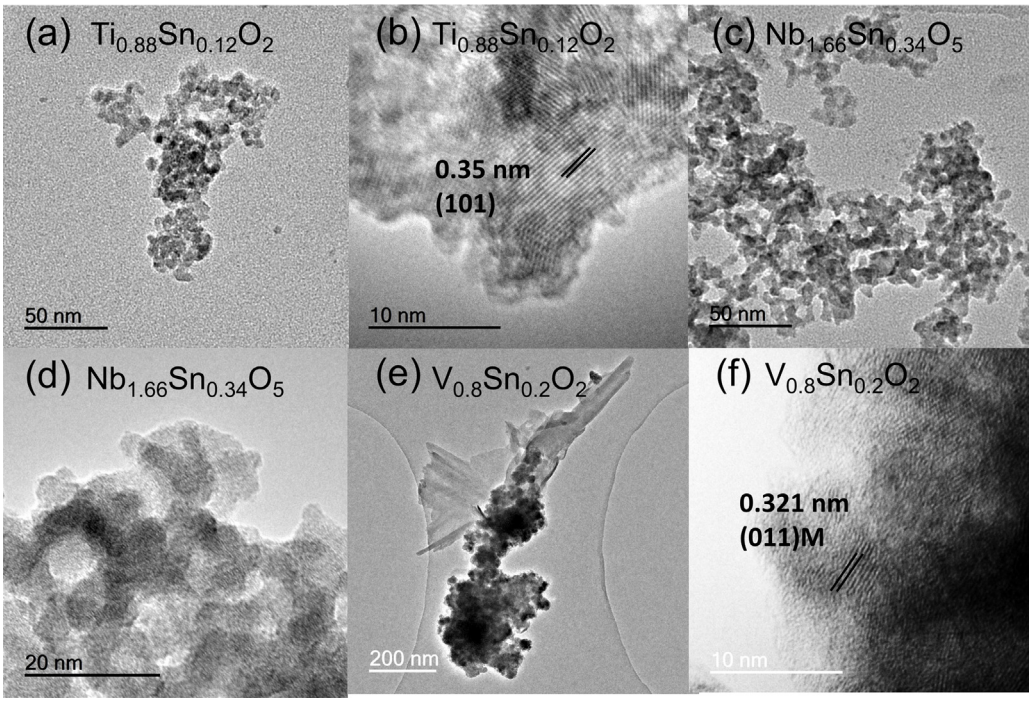

Fig. 2. TEM and HRTEM of $Ti_{0.88}Sn_{0.12}O_2$ [a) and b)], $Nb_{1.66}Sn_{0.34}O_5$ [c) and d)] and $V_{0.8}Sn_{0.2}O_2$ [e) and f)].

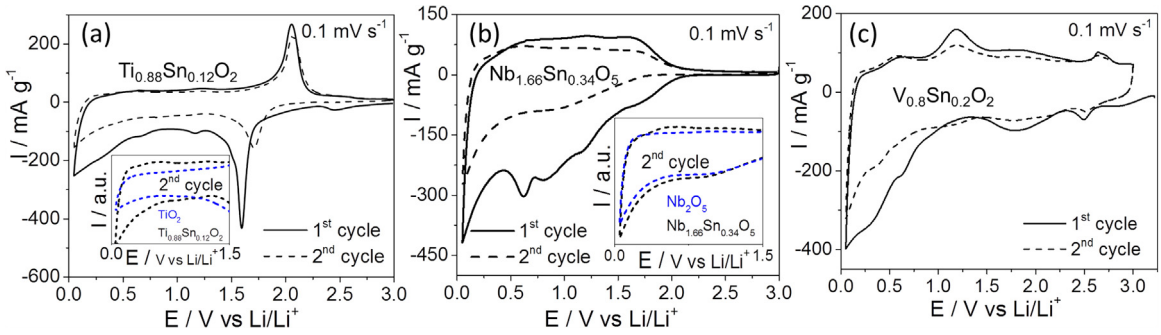

Fig. 3. Cyclic voltammograms at 0.1 mV s^{-1} of a) $Ti_{0.88}Sn_{0.12}O_2$ (inset shows comparison with undoped TiO_2 between 1.5 to 0.05 V *vs* Li/Li^+), b) $Nb_{1.66}Sn_{0.34}O_5$ (inset shows comparison with undoped Nb_2O_5 between 1.5 to 0.05 V *vs* Li/Li^+) and c) $V_{0.8}Sn_{0.2}O_2$.

For the $V_{0.8}Sn_{0.2}O_2$ in half cells, the CV profile was not very well defined at each potential, which was likely to be due to the material being mixed phase and nano-sized [7]. In the potential range of 2.0 to 3.0 V *vs* Li/Li^+, there were two reversible minor peaks, which could be attributed to lithium-ion insertion into VO_2 [4,51], but overall, as for the niobium oxide based material, the charge storage could be largely defined as being "pseudocapacitive with some insertion" [6,7]. The CV showed a delithiation peak at ca. 0.55 V *vs* Li/Li^+ (tentatively assigned to back dealloying reaction of Eq. (4)). There was an important difference in the CV for $V_{0.8}Sn_{0.2}O_2$, which was not seen for the other two doped materials or the undoped VO_2 (see supplementary Fig. S6), which was an additional delithiation peak at ca. 1.18 V *vs* Li/Li^+. This peak at 1.18 V *vs* Li/Li^+ may relate to the back reaction for Eq. (3) and would be comparable to the CV peak of highly dispersed SnO_2 in a very conductive electrode network, as reported recently by Shen et al. [52], Srinivasan et al. [53] and Liang et al. [54]. Though, more evidence is needed in future to fully confirm this suggestion for the $V_{0.8}Sn_{0.2}O_2$ sample.

In Fig. 4, the first two cycles were plotted for a galvanostatic measurement at 50 mA g^{-1} *via* a potential versus capacity plot. The irreversible capacity loss (ICL) during the first cycle was *ca.* 260 mAh g^{-1} for $Ti_{0.88}Sn_{0.12}O_2$ and *ca.* 700 mAh g^{-1} for $Nb_{1.66}Sn_{0.34}O_5$. The high surface area of each material was expected to increase the quantity of the electrolyte side reactions for initial solid electrolyte interphase (SEI) formation [55]. Moreover, if the conversion reaction is considered irreversible, this would drastically increase the lithium-ion loss during the first lithiation. Interestingly, the $V_{0.8}Sn_{0.2}O_2$ cell was able to store 1050 mAh g^{-1} during the first lithiation and showed a higher reversibility as a percentage (irreversible capacity loss of *ca.* 300 mAh g^{-1}), which resulted in high specific capacities after the first cycle. The authors thus, tentatively suggest that this could be an indication for partial back reactions towards Sn^{4+} (Eq. (3)), as seen for the CV (but further investigations, probably of an in situ nature, *e.g.* in situ CV and XPS, would be needed for a definitive assignment).

C-rate tests were performed and the data is shown in Fig. 5a–c, the following named capacities are referred to the fifth cycle at each applied current density. Undoped TiO_2 had a specific capacity of 170 mAh g^{-1} and for $Ti_{0.88}Sn_{0.12}O_2$ it was 235 mAh g^{-1} (at 100 mA g^{-1}) in the potential range of 0.05 to 3.00 V *vs* Li/Li^+; the increased lithium-ion storage was due to the electrochemical activity of the Sn^{4+} atoms. $Ti_{0.88}Sn_{0.12}O_2$, showed specific capacities at different current rates, *e.g.* 235 mAh g^{-1} at 100 mA g^{-1}, 146 mAh g^{-1} at 500 mA g^{-1}, 110 mAh g^{-1} at 1,000 mA g^{-1} and 90 mAh g^{-1} at 2,000 mA g^{-1} (see Fig. 5a). The Coulombic efficiency was in the range 87 - 95 % at 100 mA g^{-1}, >98.8 % at 500 mA g^{-1} and >99.6 % at even higher currents. The capacity remained stable (compared to pure SnO_2 materials) during the subsequent 100 cycles at 500 mA g^{-1}, with a Coulombic efficiency of >99 % and a capacity retention of 84 % (from 152 to 129 mAh g^{-1}), Fig. 5d. This capacity retention is quite low compared to pure anatase TiO_2, which is known to be able to cycle with nearly no decay [56,57], but is still very high compared to pure SnO_2 based materials, which tend to show huge capacity decay during the first 20 cycles [26,58].

Undoped Nb_2O_5 had a specific capacity of 191 mAhg^{-1} and $Nb_{1.66}Sn_{0.34}O_2$ showed 272 mAh g^{-1} (at 100 mA g^{-1}). The specific capacities of $Nb_{1.66}Sn_{0.34}O_5$ at different current rates were 272 mAh g^{-1} at 100 mA g^{-1}, 181 mAh g^{-1} at 500 mA g^{-1}, 146 mAh g^{-1} at 1,000 mA g^{-1} and 110 mAh g^{-1} at 2,000 mA g^{-1}, (see Fig. 5b). The Coulombic efficiency value was <95 % at 100 mA g^{-1}, >98.5 % at 500 mA g^{-1} and >99.4 % at higher current rates. The capacity remained stable during the following cycles at 500 mA g^{-1} with a Coulombic efficiency of >99 % and a capacity retention of 86 % (from 178 to 154 mAh g^{-1}), Fig. 5e. The cycle stability was lower than that reported in the authors' previous report for Nb_2O_5, where a retention of 98.6 % was observed after 800 cycles at the same current rate [6].

The C-rate test for $V_{0.8}Sn_{0.2}O_2$ is presented in Fig. 5c, with obtained capacities of 673 mAh g^{-1} at 100 mA g^{-1}, 607 mAh g^{-1} at 500 mA g^{-1}, 560 mAh g^{-1} at 1,000 mA g^{-1} and 515 mAh g^{-1} at 2,000 mA g^{-1}. These were far higher than undoped VO_2, which had

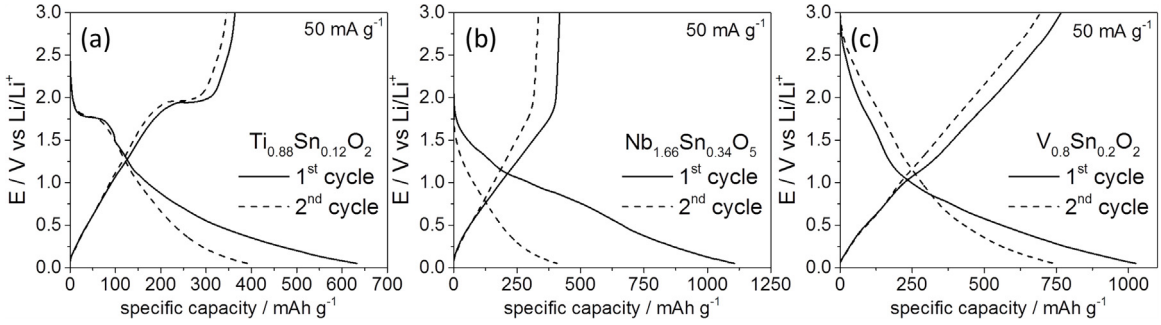

Fig. 4. First two cycles plotted *via* a potential versus capacity plot (at 50 mA g^{-1}) for a) $Ti_{0.88}Sn_{0.12}O_2$, b) $Nb_{1.66}Sn_{0.34}O_5$ and c) $V_{0.8}Sn_{0.2}O_2$.

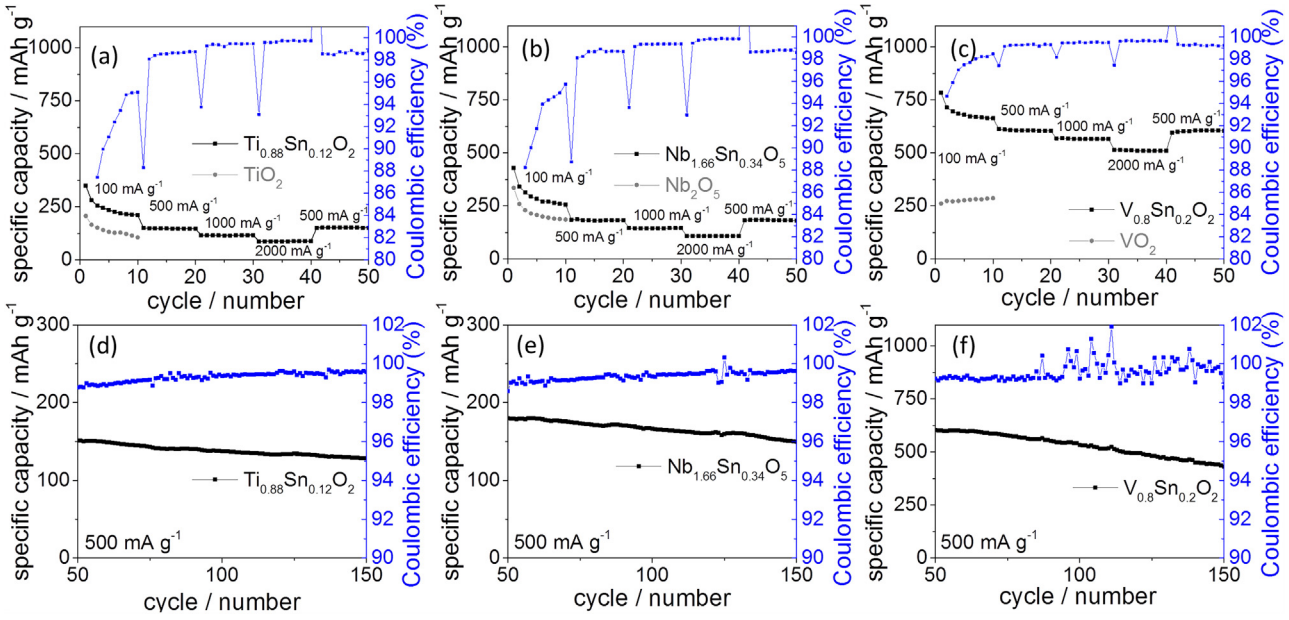

Fig. 5. C-rate test at various current rates for a) $Ti_{0.88}Sn_{0.12}O_2$, b) $Nb_{1.66}Sn_{0.34}O_5$ and c) $V_{0.8}Sn_{0.2}O_2$ (Coulombic efficiency of first two cycles not shown). The C-rate tests were followed by long term cycling at 500 mA g^{-1} for d) $Ti_{0.88}Sn_{0.12}O_2$, e) $Nb_{1.66}Sn_{0.34}O_5$ and f) $V_{0.8}Sn_{0.2}O_2$.

a specific capacity of 255 mAh g^{-1} at 100 mA g^{-1}. The Coulombic efficiency was <97 % (after 4 cycles) at 100 mA g^{-1} and >99.5 % at higher currents. The capacity remained relatively unstable during the subsequent 100 cycles at 500 mA g^{-1}, with capacity retention of 71 %, i.e. going from 608 to 432 mAh g^{-1} (Fig. 5f). The cycling stability is lower than expected when comparing to an insertion undoped VO_2 material under these cycling conditions [7,59]. Cycling at 50 mA g^{-1}, resulted in a specific capacity of 634 mAh g^{-1} after 25 cycles (see supplementary Fig. S8).

Considering that the Sn-atoms in the TiO_2 Nb_2O_5 and VO_2-based materials remained electrochemically active during cycling, the limited cycle stability might be overall due to significant contributions from alloying of the Sn component in the materials, which can lead to significant local volume changes that affect microstructure (giving deleterious effects on capacity retention) and that normally give huge capacity decay during cycling [56,57]. Thus, considering the Sn content in the doped materials, they were in fact able to cycle and retain some capacity compared to pure SnO_2.

Overall it can be concluded that the use of Sn-atoms in nano-sized insertion transition metal oxides, can increase the specific capacity because of the electrochemical activity of the Sn^{4+}. Furthermore, in the Sn doped V^{4+}-based material, there is a significantly higher capacity compared to the other two. The additional delithiation peak at 1.20 V *vs* Li/Li^+ remained relatively stable during cycling (as shown in supplementary Fig. S7, where the reaction plateau remained stable after 5 cycles). This was very different to the CVs of the TiO_2 and Nb_2O_5 based doped Sn materials (which showed no peak in this area and also less capacity win), which could suggest that this peak is important in accounting for the anomalously high capacity seen in the doped V oxide. VO_2 is a known excellent electronic conductor and V^{4+} is a good matrix element for alloying-based materials, which has been noted in previous reports by Reddy et al.[60–62]. The electronic properties of VO_2 and maybe also the slightly lower active loading, could have led to increased electron transport (which is known to be the main driving force for conversion reactions) [63,64]. The low Coulombic efficiencies for $Ti_{0.88}Sn_{0.12}O_2$, $Nb_{1.66}Sn_{0.34}O_5$ and $V_{0.8}Sn_{0.2}O_2$ might be expected, as a stable SEI for high surface area transition metal oxides, is questionable and was observed by the authors before [6,7,35], see also [15,65]. Electrolyte additives might help improve this further in the future [66,67]. A key question in this report is the origin of the higher than expected capacity for the $V_{0.8}Sn_{0.2}O_2$ material, for which there are several options that will require further investigations in the future to confirm (possibly via in situ measurements). The authors however, expect that some of the following will be the reasons for the higher than expected capacity for the doped V materials; (i) there could be reversible conversion reactions for Sn^{4+} based alloying materials as discussed before, (ii) there might be some impact from particle cracking (which causes higher surface area, leading to increased lithium-ion storage sites) [68,69] and also possibly (iii) there might be an impact of charge storage from LiO_2/LiOH layers, which form reversibly (which are first formed during the first lithiation) [30–32]. Therefore, the overall charge storage mechanism, in particular for sample $V_{0.8}Sn_{0.2}O_2$, is quite complex and will warrant further detailed and in situ or post-cycling investigation in the future. Considering the author's previous results for Sn-doped TiO_2 [20] (Sn-loading in TiO_2 proportionally increases the delithiation peak at 0.55 V *vs* Li/Li^+ and therefore increases the specific capacity) and the observed capacity storage and release at lower potentials (where Sn is known to be active), it is suggested that all doped materials showed increased charge storage due to the alloying reaction of the Sn-dopant.

The literature contains many examples of Sn-based materials, which have been mixed with other carbons or transition metal oxides, some of which require multistep syntheses, *e.g.* core/shell [70], carbon/alloying [29,71], hollow nano-spheres [72], and others [18]. The benefit of the approach used herein, is in the scalability and ease of the synthesis process in a single and direct step. Furthermore, these initial results are promising because they describe materials that are clearly capable of combined insertion and alloying charge storage processes with reasonable stability compared to purely alloying (only) materials and showing high capacities compared to insertion (only) materials.

4. Conclusions

$Ti_{0.88}Sn_{0.12}O_2$, $Nb_{1.63}Sn_{0.34}O_5$ and $V_{0.8}Sn_{0.2}O_2$ were synthesized in a single step via a pilot scale CHFS hydrothermal reactor at a production rate of at least 65 g h^{-1}. The obtained nanomaterials were directly investigated as potential negative electrode

materials in lithium-ion battery half-cells in the potential range of 0.05 to 3.00 V *vs* Li/Li^+. The specific capacities at 100 mA g^{-1} were 235, 272 and 673 mAh g^{-1} for $Ti_{0.88}Sn_{0.12}O_2$, $Nb_{1.66}Sn_{0.34}O_5$ and $V_{0.8}Sn_{0.2}O_2$, respectively, which were each higher compared to the undoped transition metal oxides. They also offered higher cycling stabilities compared to pure alloying materials alone. In particular, the electrochemical performance of the Sn-doped vanadium oxide ($V_{0.8}Sn_{0.2}O_2$) electrode delivered an unexpectedly high and stable specific capacity of 630 mAh g^{-1} at an applied current of 50 mA g^{-1} (over 25 cycles) and showed promising high-rate performance (capacity of 515 mAh g^{-1} at 2 A g^{-1}). Overall, these results suggest, that doping nano-sized insertion metal oxide host lattices with significant amounts of tin, can increase the stored capacity due to additional charge storage via lithium alloying reactions associated a Sn metal phase that is presumed to form at lower potentials vs Li/Li^+.

Acknowledgements

The EPSRC are thanked for funding the Centre for Doctoral Training in Molecular Modelling & Materials Science (UCL, UK) and A Star (Singapore) are thanked for supporting a studentship for ML and AJG. Mr Joe Nolan is thanked for technical support. Diana Teixeira, UCL, is thanked for SEM measurements and fruitful discussions. Dustin Bauer (UCL) is thanked for additional electrochemical investigations. Special thanks to Professor B V R Chowdari, Department of Physics, National University of Singapore, for the use of his laboratories in processing these coin cells.

Appendix A. Supplementary data

Supplementary data associated with this article can be found, in the online version, at http://dx.doi.org/10.1016/j.electacta.2017.02.063.

References

[1] M. Winter, R.J. Brodd, Chemical reviews 104 (2004) 4245–4270.
[2] I. Hadjipaschalis, A. Poullikkas, V. Efthimiou, Renewable and Sustainable Energy Reviews 13 (2009) 1513–1522.
[3] M.V. Reddy, G.V. Subba Rao, B.V.R. Chowdari, Chem. Rev. 113 (2013) 5364–5457.
[4] N.A. Chernova, M. Roppolo, A.C. Dillon, M.S. Whittingham, Journal of Materials Chemistry 19 (2009) 2526–2552.
[5] L. Mai, L. Xu, C. Han, X. Xu, Y. Luo, S. Zhao, Y. Zhao, Nano letters 10 (2010) 4750–4755.
[6] M. Lübke, A. Sumboja, I.D. Johnson, D.J. Brett, P.R. Shearing, Z. Liu, J.A. Darr, Electrochimica Acta 192 (2016) 363–369.
[7] M. Lübke, N. Ding, M.J. Powell, D.J. Brett, P.R. Shearing, Z. Liu, J.A. Darr, Electrochemistry Communications 64 (2016) 56–60.
[8] M. Lübke, J. Shin, P. Marchand, D. Brett, P. Shearing, Z. Liu, J.A. Darr, Journal of Materials Chemistry A 3 (2015) 22908–22914.
[9] Q. Zhao, L. Jiao, W. Peng, H. Gao, J. Yang, Q. Wang, H. Du, L. Li, Z. Qi, Y. Si, Y. Wang, H. Yuan, Journal of Power Sources 199 (2012) 350–354.
[10] C. Nethravathi, B. Viswanath, J. Michael, M. Rajamath, Carbon 50 (2012) 4839–4846.
[11] C. Nethravathi, C.R. Rajamathi, M. Rajamathi, U.K. Gautam, X. Wang, D. Golberg, Y. Bando, ACS applied materials & interfaces 5 (2013) 2708–2714.
[12] L. Mai, Q. Wei, Q. An, X. Tian, Y. Zhao, X. Xu, L. Xu, L. Chang, Q. Zhang, Advanced Materials 25 (2013) 2969–2973.
[13] C. Niu, J. Meng, C. Han, K. Zhao, M. Yan, L. Mai, Nano letters 14 (2014) 2873–2878.
[14] X. Tian, X. Xu, L. He, Q. Wei, M. Yan, L. Xu, Y. Zhao, C. Yang, L. Mai, Journal of Power Sources 255 (2014) 235–241.
[15] W.-J. Zhang, Journal of Power Sources 196 (2011) 13–24.
[16] M.R. Palacin, Chemical Society Reviews 38 (2009) 2565–2575.
[17] L. Croguennec, M.R. Palacin, Journal of the American Chemical Society 137 (2015) 3140–3156.
[18] H. Wang, H. Huang, C. Niu, A.L. Rogach, small 11 (2015) 1364–1383.
[19] D. Deng, M.G. Kim, J.Y. Lee, J. Cho, Energy & Environmental Science 2 (2009) 818–837.
[20] M. Lübke, I. Johnson, N.M. Makwana, D. Brett, P. Shearing, Z. Liu, J.A. Darr, Journal of Power Sources 294 (2015) 94–102.
[21] Z. Yang, D. Choi, S. Kerisit, K.M. Rosso, D. Wang, J. Zhang, G. Graff, J. Liu, Journal of Power Sources 192 (2009) 588–598.
[22] J.S. Chen, Y.L. Cheah, Y.T. Chen, N. Jayaprakash, S. Madhavi, Y.H. Yang, X.W. Lou, The Journal of Physical Chemistry C 113 (2009) 20504–20508.
[23] M.S. Park, Y.M. Kang, G.X. Wang, S.X. Dou, H.K. Liu, Advanced Functional Materials 18 (2008) 455–461.
[24] Y.-D. Ko, J.-G. Kang, J.-G. Park, S. Lee, D.-W. Kim, Nanotechnology 20 (2009) 455701.
[25] R. Demir-Cakan, Y.-S. Hu, M. Antonietti, J. Maier, M.-M. Titirici, Chemistry of Materials 20 (2008) 1227–1229.
[26] Y. Wang, Z.X. Huang, Y. Shi, J.I. Wong, M. Ding, H.Y. Yang, Scientific Reports 5 (2015) 9164.
[27] D. Mhamane, V. Aravindan, D. Taneja, A. Suryawanshi, O. Game, M. Srinivasan, S. Ogale, Composites Science and Technology 130 (2016) 88–95.
[28] Z. Chen, M. Zhou, Y. Cao, X. Ai, H. Yang, J. Liu, Advanced Energy Materials 2 (2012) 95–102.
[29] X. Guo, X. Fang, Y. Sun, L. Shen, Z. Wang, L. Chen, Journal of Power Sources 226 (2013) 75–81.
[30] S.-Y. Lee, K.-Y. Park, W.-S. Kim, S. Yoon, S.-H. Hong, K. Kang, M. Kim, Nano Energy 19 (2016) 234–245.
[31] Y.-Y. Hu, Z. Liu, K.-W. Nam, O.J. Borkiewicz, J. Cheng, X. Hua, M.T. Dunstan, X. Yu, K.M. Wiaderek, L.-S. Du, Nature materials 12 (2013) 1130–1136.
[32] D. Aurbach, Journal of Power Sources 89 (2000) 206–218.
[33] M. Lübke, N.M. Makwana, R. Gruar, C. Tighe, D. Brett, P. Shearing, Z. Liu, J.A. Darr, Journal of Power Sources 291 (2015) 102–107.
[34] H. Hayashi, T. Nakamura, T. Ebina, Journal of the Ceramic Society of Japan 122 (2014) 78–82.
[35] M. Lübke, P. Marchand, D.J. Brett, P. Shearing, R. Gruar, Z. Liu, J.A. Darr, Journal of Power Sources 305 (2016) 115–121.
[36] I.D. Johnson, M. Lübke, O.Y. Wu, N.M. Makwana, G.J. Smales, H.U. Islam, R.Y. Dedigama, R.I. Gruar, C.J. Tighe, D.O. Scanlon, Journal of Power Sources 302 (2016) 410–418.
[37] M.J. Powell, P. Marchand, C. Denis, J. Bear, J. Darr, I. Parkin, Nanoscale 7 (2015) 18686–18693.
[38] R.I. Gruar, C.J. Tighe, J.A. Darr, Ind. Eng. Chem. Res. 52 (2013) 5270–5281.
[39] Y. Hakuta, H. Terayama, S. Onai, T. Adschiri, K. Arai, Proc 4th Int. Symp. on 'Supercritical Fluids, 'sendai, Japan, May, 1997, pp. 255–258.
[40] J. Parker, Physical Review B 42 (1990) 3164.
[41] M. Shirpour, J. Cabana, M. Doeff, Energy & Environmental Science 6 (2013) 2538–2547.
[42] A. Rudola, K. Saravanan, C.W. Mason, P. Balaya, Journal of Materials Chemistry A 1 (2013) 2653–2662.
[43] Y. Wang, M. Xu, Z. Peng, G. Zheng, Journal of Materials Chemistry A 1 (2013) 13222–13226.
[44] H. Wang, L. Xi, J. Tucek, C. Ma, G. Yang, M.K. Leung, R. Zboril, C. Niu, A.L. Rogach, ChemElectroChem 1 (2014) 1563–1569.
[45] A.L. Viet, M. Reddy, R. Jose, B. Chowdari, S. Ramakrishna, The Journal of Physical Chemistry C 114 (2009) 664–671.
[46] H. Luo, M. Wei, K. Wei, Materials Chemistry and Physics 120 (2010) 6–9.
[47] H. Wen, Z. Liu, J. Wang, Q. Yang, Y. Li, J. Yu, Applied Surface Science 257 (2011) 10084–10088.
[48] A. Le Viet, M.V. Reddy, R. Jose, B.V.R. Chowdari, S. Ramakrishna, Electrochimica Acta 56 (2011) 1518–1528.
[49] J.W. Kim, V. Augustyn, B. Dunn, Advanced Energy Materials 2 (2012) 141–148.
[50] J. Come, V. Augustyn, J.W. Kim, P. Rozier, P.-L. Taberna, P. Gogotsi, J.W. Long, B. Dunn, P. Simon, Journal of The Electrochemical Society 161 (2014) A718–A725.
[51] W. Zhang, L. Shi, K. Tang, Y. Yu, Chemistry Letters 41 (2012) 104–106.
[52] L. Shen, F. Liu, G. Chen, H. Zhou, Z. Le, H.B. Wu, G. Wang, Y. Lu, Journal of Materials Chemistry A 4 (2016) 18706–18710.
[53] N.R. Srinivasan, S. Mitra, R. Bandyopadhyaya, Physical Chemistry Chemical Physics 16 (2014) 6630–6640.
[54] J. Liang, X.Y. Yu, H. Zhou, H.B. Wu, S. Ding, X.W.D. Lou, Angewandte Chemie International Edition 53 (2014) 12803–12807.
[55] J.Y. Shin, D. Samuelis, J. Maier, Advanced Functional Materials 21 (2011) 3464–3472.
[56] J. Chen, H. Hou, Y. Yang, W. Song, Y. Zhang, X. Yang, Q. Lan, X. Ji, Electrochimica Acta 164 (2015) 330–336.
[57] D. Bresser, G.-T. Kim, E. Binetti, M. Striccoli, R. Comparelli, S. Seidel, D. Ozkaya, M. Copley, P. Bishop, E. Paillard, S. Passerini, Journal of Power Sources 294 (2015) 406–413.
[58] K. Zhao, L. Zhang, R. Xia, Y. Dong, W. Xu, C. Niu, L. He, M. Yan, L. Qu, L. Mai, Small 12 (2016) 588–594.
[59] G. He, L. Li, A. Manthiram, Journal of Materials Chemistry A 3 (2015) 14750–14758.
[60] M. Reddy, V. Khai, B. Chowdari, Solid State Ionics 268 (2014) 277–281.
[61] M. Reddy, G.S. Rao, B. Chowdari, Journal of Materials Chemistry 21 (2011) 10003–10011.
[62] B. Das, M. Reddy, G.S. Rao, B. Chowdari, Journal of Solid State Electrochemistry 15 (2011) 259–268.
[63] F. Wang, R. Robert, N.A. Chernova, N. Pereira, F. Omenya, F. Badway, X. Hua, M. Ruotolo, R. Zhang, L. Wu, Journal of the American Chemical Society 133 (2011) 18828–18836.
[64] L. Li, F. Meng, S. Jin, Nano letters 12 (2012) 6030–6037.
[65] S. Goriparti, E. Miele, F. De Angelis, E. Di Fabrizio, R. Proietti Zaccaria, C. Capiglia, Journal of Power Sources 257 (2014) 421–443.

[66] K. Abe, H. Yoshitake, T. Kitakura, T. Hattori, H. Wang, M. Yoshio, Electrochimica acta 49 (2004) 4613–4622.
[67] L. Chen, K. Wang, X. Xie, J. Xie, Journal of Power Sources 174 (2007) 538–543.
[68] W.J. Borghols, M. Wagemaker, U. Lafont, E.M. Kelder, F.M. Mulder, Chemistry of Materials 20 (2008) 2949–2955.
[69] K.T. Lee, J. Cho, Nano today 6 (2011) 28–41.
[70] J.Y. Liao, A. Manthiram, Advanced Energy Materials 4 (2014).
[71] Y. Xu, Q. Liu, Y. Zhu, Y. Liu, A. Langrock, M.R. Zachariah, C. Wang, Nano letters 13 (2013) 470–474.
[72] J.S. Chen, L.A. Archer, X.W.D. Lou, Journal of Materials Chemistry 21 (2011) 9912–9924.